Draft version September 5, 2024
Typeset using LATEX twocolumn style in AASTeX631

Rising from the Ashes II: A Hidden Abundance Bimodality in Illustris TNG

Angus Beane,[1] James W. Johnson,[2] and et al

[1]Center for Astrophysics | Harvard & Smithsonian, Cambridge, MA, USA
[2]The Observatories of the Carnegie Institution for Science, Pasadena, CA, USA

ABSTRACT

The Milky Way is known to host at least two modes in the present day distribution of Fe and α-elements. The exact cause of this bimodality is disputed, but one class of explanations involves the merger between the Milky Way and a relatively massive sattelite (Gaia-Sausage-Enceladus) at $z \sim 2$. However, reproducing this bimodality in simulations is not straightforward, with conflicting results on the prevalance, morphology, and mechanism behind multimodality. We present a case study of a galaxy in the Illustris TNG50 simulation which undergoes a sequence of starburst, brief quiescence, and then rejuvenation. After a minor post-processing step which boosts the $[\alpha/\mathrm{Fe}]$ of old star particles, we demonstrate that this galaxy hosts a strongly bimodal distribution in the $[\alpha/\mathrm{Fe}]$-$[\mathrm{Fe}/\mathrm{H}]$ plane. The high- and low-α sequences are neatly separated in time by the brief quiescent period. The quiescent period in this galaxy is not associated with a merger but some unspecified internal process which leads to AGN activity. We argue that the post-processing step can be understood as the TNG model underproducing star formation in the densest regions at high-z.

Keywords: Classical Novae (251) — Ultraviolet astronomy(1736) — History of astronomy(1868) — Interdisciplinary astronomy(804)

1. INTRODUCTION

The stellar surface abundances of most elements retain the composition of their natal gas cloud. Therefore, the present-day distribution of stellar surface abundances encodes the chemical history of a galaxy's gas phase. Two elements have received particular interest in the Milky Way: Fe and α-elements (elements produced through the α-process, such as O and Mg). Fe is produced in both Type Ia and Type II SNe whereas α-elements are produced predominantly through Type II SNe. Because these SNe occur on different timescales (10s of Myr after star formation for Type II, as compared to 100s of Myr to Gyrs for Type Ia), the ratio between α-elements and Fe is expected to generally decrease with time.

Because of their separate formation channels, the two dimensional plane of $[\alpha/\mathrm{Fe}]$-$[\mathrm{Fe}/\mathrm{H}]$ has received considerable interest. In the Milky Way, there is a well-established bimodality with separate high- and low-α sequences (Gratton et al. 1996; Fuhrmann 1998, 2004; Reddy et al. 2006; Adibekyan et al. 2011, 2012; Bensby et al. 2014; Nidever et al. 2014; Hayden et al. 2020). This bimodal distribution is shown in the upper left panel of Figure 1.

A more extensive survey of the different proposed formation mechanisms of this bimodality is given in Beane (2024). Here, we mention simply that there are two approaches. First, the bimodality is a result of internal secular processes that generate the bimodality through radial migration (Schönrich & Binney 2009; Sharma et al. 2021; Chen et al. 2023) or clump formation (Clarke et al. 2019; Beraldo e Silva et al. 2020, 2021; Garver et al. 2023).

Second, the bimodality is generated through gas infall scenarios, either from specific gas accretion episodes from the intergalactic medium (Chiappini et al. 1997; Chiappini 2009; Grisoni et al. 2017; Spitoni et al. 2019), or through a more self-consistent collapse sequence of the circumgalactic medium driven through feedback (Khoperskov et al. 2021). Third and finally, the bimodality is generated through a merger process, either by enhancing the SFR of the Galaxy (Brook et al. 2004, 2005, 2007; Richard et al. 2010) or by supplying a relatively pristine gas supply that resets the metallicity of the Galaxy (Buck 2020; Ciucă et al. 2024). The fact that the Milky Way did undergo a merger with the Gaia-Sausage-Enceladus (GSE) satellite supports these scenarios (Belokurov et al. 2018; Helmi et al. 2018; Naidu et al. 2020).

In Beane (2024) we argued for an alternate formation scenario of the bimodality, for which we provide further support in this work. In this scenario, the bimodality is formed through a brief quiescent period in the Galaxy's history. During this period, which lasted ~ 300 Myr in that setup, two things happen. First, as the chemical evolution of the galaxy proceeds, fewer stars form. Second, because the SFR is lower, α-element production drops and so the $[\alpha/\mathrm{Fe}]$ of the gas drops as well. The combination of these two effects is what leads to the valley in between the high- and low-α sequences.

In that work, we used idealized simulations of a galaxy merger that triggered a starburst which preceded the quiescent period. However, we argued that the merger aspect of that work was not necessary, but rather the quiescence. In this work, we study a subhalo from the Illustris TNG50 simulation which demonstrates this. This subhalo of interest (SoI) exhibits the sequence of events presented in Beane (2024) after a simple post-processing step which enhances the $[\alpha/\mathrm{Fe}]$ of old star particles. The SoI undergoes a brief quiescent period which neatly separates a high- and low-α sequence. Therefore, this work serves as a verification that the scenario in Beane (2024) is possible in cosmological simulations and can occur in non-merger scenarios.

In Section 2 we discuss our selection technique which led to discovering the SoI, as well as a simple one zone chemical evolution model we use to justify our post-processing step. In Section 3 we present the main results which we discuss and interpret in Section 4. We conclude in Section 5.

2. METHODS

2.1. *IllustrisTNG Sample*

We have made use of the Illustris TNG50 simulation (Pillepich et al. 2019; Nelson et al. 2019), a cosmological simulation of a $\sim 50\,\mathrm{cMpc}$ box at high resolution ($m_{\mathrm{baryon}} \sim 8.5 \times 10^4\,M_\odot$). It uses the gravito-magneto-hydrodynamics code `AREPO` (Springel 2010; Pakmor et al. 2016), along with the TNG model (Vogelsberger et al. 2013; Weinberger et al. 2017; Pillepich et al. 2018). This model includes several subgrid processes: a wind generation model, chemical enrichment from supernovae and asymptotic giant branch stars, and thermal and kinetic feedback from AGN.

Using the public catalog, we selected a sample of subhalos at $z = 1.5$ (snapshot 40) according to the following criteria: (1) the subhalo is central (i.e., the most massive subhalo within its halo), and (2) the subhalo's stellar mass is between 10^{10} and $10^{10.5}\,M_\odot/\mathrm{h}$. There were a total of 168 subhalos that met both criteria. The chosen mass range is broadly consistent with the expected mass of the Milky Way at this redshift (van Dokkum et al. 2013). We chose to make our selection of galaxies at $z = 1.5$ instead of at lower redshift because we wished to capture the *formation* of any multimodal structure. We did not want contamination by mergers at lower redshift which we know contribute very little to the Milky Way's disk stars (e.g., Bland-Hawthorn & Gerhard 2016).

We examined the abundance distribution in the [Mg/Fe]-[Fe/H] plane of this sample of subhalos by eye. Not many subhalos had multimodal structure, and any structure that was present was relatively weak compared to that observed in the Milky Way. We then applied a post-processing to the [Mg/Fe] of stars by adding to each star particle a value of $0.1 \times (t_{1.5} - t_{\mathrm{form}})$, where $t_{1.5}$ is the age of the universe at $z = 1.5$ ($\sim 4.3\,\mathrm{Gyr}$) and t_{form} is the formation time of each star particle. With this post-processing, we found that much more structure was generally present. We selected subhalo 172175 (at snapshot 40) for its particular resemblance to the Milky Way. We then studied the main descendant of this subhalo at $z = 0$ (subhalo 392276 at snapshot 99). We refer to this subhalo as our subhalo of interest (SoI).

2.2. *Observations*

We make use of two observational data sets. First, we use the ASPCAP DR17 catalog of stellar abundances (García Pérez et al. 2016, J.A. Holtzman et al., in preparation). We make the same selection cuts as in Beane (2024), described in their Section 2.4. These are meant to select only giants with high quality abundance measurements as well as restricting the sample to only stars in the disk with angular momenta similar to the Sun's. This results in a sample of 54,777 stars. We use Fe to track total metallicity and Mg alone as an α-element.

We then further considered a dataset of stellar ages from the APOKASC2 catalog (Pinsonneault et al. 2018). This uses a combination of APOGEE spectroscopic parameters and *Kepler* time series photometry to compute astroseismic ages. We cross-match this catalog to our larger sample from ASPCAP which results in a sample of 1868 stars.

2.3. *One-Zone Chemical Evolution Model*

James inserts his section

3. RESULTS

3.1. *Abundance Plane*

The main result of our paper is given in Figure 1. Here, we compare the abundance plane in the Milky Way (left column) to that in our subhalo of interest (middle and right columns). The upper panels show the 2D distribution in the space of [Mg/Fe]-[Fe/H]. We have applied the standard `scipy` implementation of a gaussian kernel density estimator to a Cartesian grid of points. For each panel, we normalize so that the integral of the distribution is unity. Colors are plotted in a log scale ranging from 0.08 to $15\,\mathrm{dex}^{-2}$. Contour lines are plotted at 0.1, 1.5, and $10\,\mathrm{dex}^{-2}$.

The colored vertical lines are indicated at $[\mathrm{Fe/H}] = -0.75$, -0.5, -0.25, and 0 dex in the Milky Way, and at bins 0.25 dex higher in the simulations. The lower panels show 1D histograms of [Mg/Fe] in bins centered on these values. The bins for the Milky Way/simulations are 0.2/0.05 dex. The [Mg/Fe] values are given offsets in order to reduce overlap. The rationale for the higher plotted [Fe/H] in the simulations comes just from the empirical location of the bimodalities. The Milky Way shows a clear bimodal population, with a high-α sequence most clearly distinct from the low-α se-

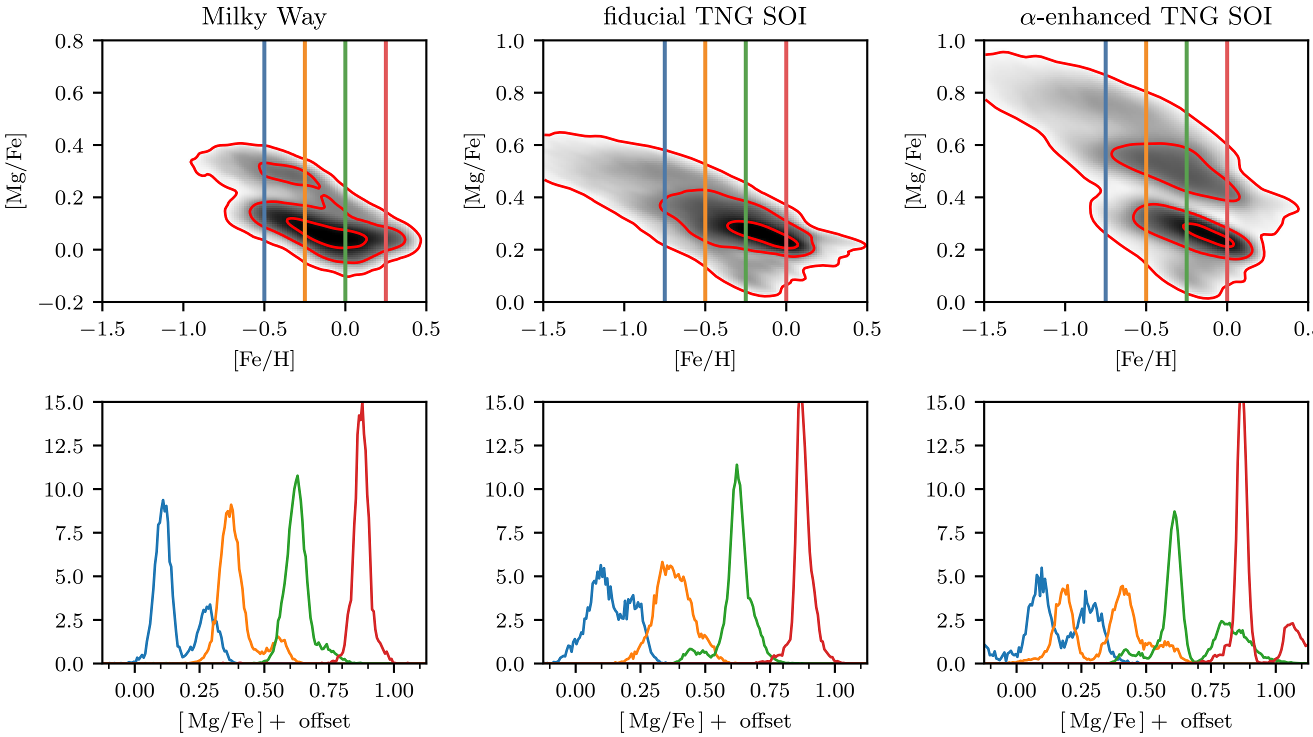

Figure 1. When old stars are α-enhanced, our subhalo of interest from TNG displays a prominent bimodality. The upper left panel shows the distribution in the [Mg/Fe]-[Fe/H] plane of the Milky Way, demonstrating a clear bimodality (data selection given in text). The lower left panel shows the 1D histograms of [Mg/Fe] at fixed [Fe/H] values of −0.5, −0.25, 0, and 0.25 (blue, orange, green, and red, respectively). In the Milky Way, the bimodality is strongest at low metallicities while disappearing at high metallicities. The middle column shows the same plots but for our TNG subhalo of interest (392276) and with the fixed [Fe/H] values 0.25 dex lower. Only faint structure is seen in the lowest bin (blue, −0.75 dex). The right column shows the same subhalo but after increasing the [Mg/Fe] value of star particles formed before $z = 1.5$ linearly with formation time (specifically by incrementing [Mg/Fe] by $0.1 \times (t_{1.5} - t_{\rm form})$ if $t_{\rm form} < t_{1.5}$, where $t_{1.5}$ is the age of the universe at $z = 1.5$). A clear bimodality is shown in these panels which, unlike in the Milky Way, is present at all metallicities.

quence at low metallicity. The two sequences merge around solar metallicity.

Our SoI, on the other hand, does not show a clearly bimodal structure in the fiducial simulation (middle column). There is some structure in the [Fe/H] = −0.75 bin. The right panel of Figure 1 shows the same distribution as in the middle panel, but with a post-processed declination in [Mg/Fe] described in Section 2.1. Star particles formed before $z = 1.5$ are given an additive offset of $0.1 \times (t_{1.5} - t_{\rm form})$, where $t_{1.5}$ is the age of the universe at $z = 1.5$ and $t_{\rm form}$ is the formation time of the star particle. A multimodal structure emerges with three clear modes at [Mg/Fe] $\sim$ 0.8, 0.5, and 0.2 dex. The 1D histograms show that the modes are well-separated, and that the troughs between the modes nearly vanish.

3.2. *Alpha Time Dependence*

The abundance distributions shown in Figure 1 can be better understood by examining the evolution of [Mg/Fe] with time of the individual stars/star particles. In the upper panels of Figure 2 we show the true distribution of [Mg/Fe] as a function of time for the fiducial SoI in the middle and for the post-processed, α-enhanced subhalo to the right. We use age instead of formation time in order to better facilitate comparisons to observations. These panels are true 2D histograms, with a logarithmic colormap normalized to the maximum of the plot. The values of [Mg/Fe] are offset to avoid overlap.

There is a gap in the ages that occurs at an age of 10.75 Gyr, which we mark with a vertical dashed line. Star particles older than this line have a much clearer gradient in time with [Mg/Fe] than stars that form after. In the [Fe/H] = −0.25 bin, star particles which form directly after this line have a slightly depressed [Mg/Fe] than stars which form a short time later.

In the lower panels we plot to the left data from the Milky Way and to the middle and right from the fiducial and α-enhanced SoI, respectively. For the simulations, we add 15% age and 0.01 dex [Mg/Fe] Gaussian errors. These values are roughly in line with the observational errors from the APOKASC2 and APOGEE datasets that the lower left panel is made from (see Appendix A for plots of the observational errors). The error in [Mg/Fe] is not signficant, but the age error, which is 1 Gyr at 10 Gyr, smears out the distribution

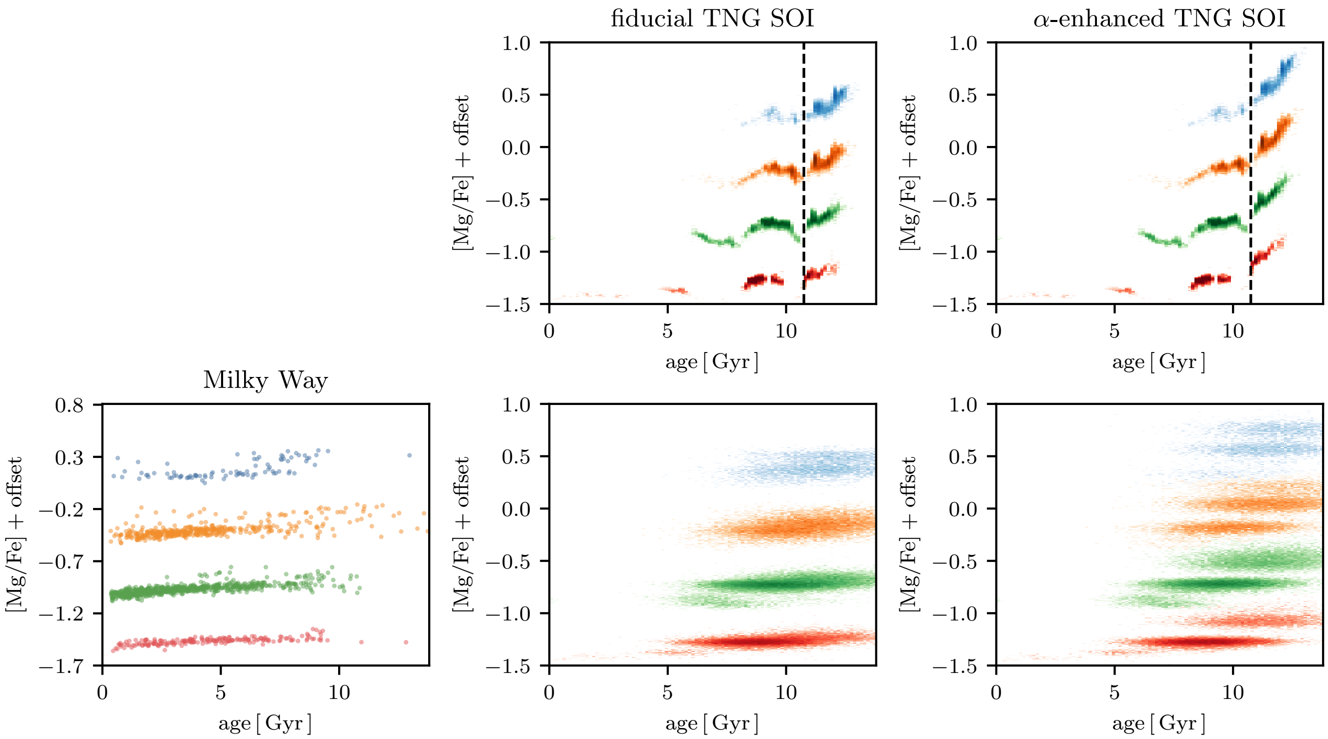

Figure 2. Bimodality in the abundance plane is linked to distinct epochs in simulation. The upper panels show [Mg/Fe] as a function of age for our subhalo in TNG. The colors indicate stellar populations at fixed values of [Fe/H], which are the same as in Figure 1. A gap in the relation occurs at an age of approximately 10.75 Gyr, which we indicate with a vertical dashed line. The effect of the α-enhancement is clear, as it separates the stars that form before and after this gap in ages (star particles which formed before $z = 1.5$ are α-enhanced, which occurs at an age of ~ 9.5 Gyr). The lower panels show on the left the Milky Way and on the center and right the data from TNG but with 15% age errors and 0.01 dex errors in [Mg/Fe]. When the simulations are given these errors, we see that the before and after star particles smear such that the two populations significantly overlap in ages. In the α-enhanced SoI, two populations emerge in each bin which overlapped in the fiducial distribution. This feature more closely resembles the Milky Way, which displays such populations where the bimodality is strongest – [Fe/H] = −0.5 (blue) and −0.25 (orange).

before and after the dashed line. The α-enhanced SoI still shows two separate populations in this plot, but they now significantly overlap in age.

The Milky Way distribution (lower left panel) bears some resemblance to the α-enhanced SoI. In particular, the [Fe/H] $= -0.5$ and -0.25 bins (blue and orange, respectively) show what appears to be two populations overlapping in age but nonetheless separated in [Mg/Fe]. These are the bins at which the bimodality is strongest (upper left panel of Figure 1).

3.3. *Evolutionary History*

In an effort towards understanding the events in our SoI's history that led to the behavior around the dashed line in Figure 2, we examine the evolution of some of its key quantities. In the upper panel of Figure 3, we show the SFH of our galaxy with the same dashed line as in Figure 2 (at an age of 10.75 Gyr in that plot is at a time of ~ 3 Gyr here). This SFH is computed from the formation times of all star particles in the subhalo at $z = 0$. This allows us to compute the SFH at fine time resolution. We see two peaks in the SFH at $t \sim 2.5$ and ~ 4.5 Gyr of an amplitude of about 70 and 60 $M_{\odot}$/yr. The dashed line corresponds to a relative drop in the SFR, down to about 10 $M_{\odot}$/yr before quickly recovering.

The middle panel shows the accretion rate of the central black hole as a fraction of the maximum (Eddington) accretion rate. Early in its history ($t < 2$ Gyr), the subhalo experiences high accretion rates. The accretion rate then steadily declines until $t \sim 5$ Gyr at which point it switches to the low accretion radio mode. However, at the dashed line (~ 3 Gyr) there is a localized peak in the accretion rate, maxing out at about 30% Eddington.

The lower panel shows the virial mass of the subhalo, as measured by M_{200} – the mass within the radius that encloses a region of density 200× the mean density of the universe. Early on at $t < 4$ Gyr the virial mass grows roughly linearly up to $\sim 2 \times 10^{12}\, M_{\odot}$. After that, the virial mass remains roughly constant until sharp increases at $t \sim 10$ and ~ 12 Gyr. The transition in the virial mass from linear to constant at $t \sim$

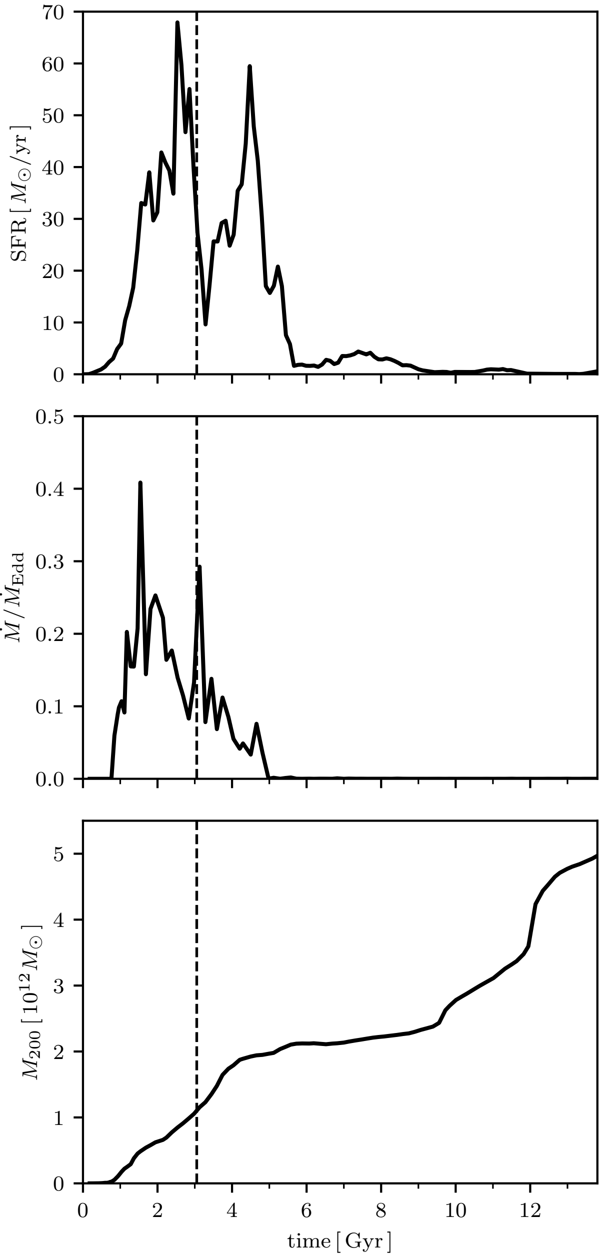

Figure 3. The evolutionary history of our subhalo of interest. The upper panel shows the SFH of our subhalo. This SFH is generated using the formation times of all star particles in the subhalo at $z = 0$. In this and all subsequent panels we show a vertical dashed line at the same position as in Figure 2 ($\sim$ 3 Gyr), which delineates the separation between the high- and low-α sequences. The gap in ages is naturally associated with a gap in the SFH located at the dashed line. The middle panel shows the BH accretion rate as a fraction of the maximum (Eddington) accretion rate across time. The accretion rate is high early on, but then drops. The gap in ages (dashed line) is coincident with a local peak in the BH accretion rate. In the lower panel we show the mass assembly of the halo, given as the mass within the radius that encloses 200× the mean density of the universe. In this plot mergers are shown as sudden increases in M_{200}. Mergers at very early times when the halo is signifcantly less massive than its $z = 0$ mass are not shown, but one can see that no clear merger is associated with the gap in stellar ages. Two mergers occur later on at $t \sim 10$ and ~ 12 Gyr.

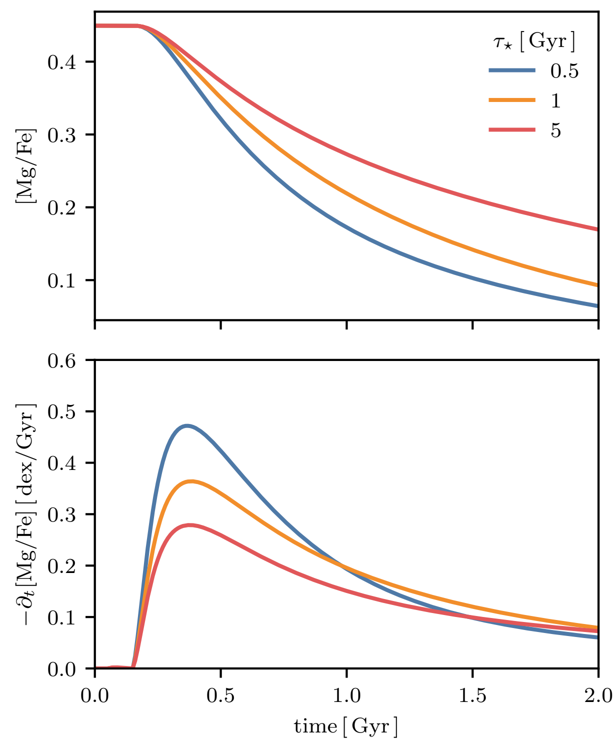

Figure 4. A higher star formation efficiency leads to a steeper decline in [Mg/Fe]. In both panels, the lines show the time evolution of [Mg/Fe] in a simple one zone chemical evolution model, described in Section 2.3. The upper panel shows the evolution of [Mg/Fe] over 2 Gyr while the lower panel shows the negative of its time derivative. Decreasing the star formation timescale $\tau_\star = M_{\rm gas/SFR}$ leads to a more rapid decline in [Mg/Fe]. At its steepest decline ($t \sim 0.5$ Gyr), an order of magnitude decrease in $\tau_\star$ leads to a slope nearly a factor of 2 larger. At later times ($t > 1$ Gyr), the models with smaller $\tau_\star$ reach their steady-state [Mg/Fe] value more quickly.

4 Gyr is followed 1 Gyr later by a sudden drop in the SFR and BH accretion rate.

3.4. *One-Zone Model*

We showed in Figure 1 that a time-linear α-enhancement of old stars (forming before $z = 1.5$) led to the emergence of a strong chemical bimodality. This α-enhancement is equivalent to saying that [α/Fe] declines more rapdily with time at high-z. In Figure 4 we demonstrate an argument for why this steeper decline in [α/Fe] might be absent in TNG.

We show in the upper panel the evolution of [Mg/Fe] of three one zone chemical evolution models which vary the star formation (SF) timescale. This timescale, $\tau_\star$, is the inverse of the SF efficiency. A shorter SF timescale leads to a more rapid reduction in [Mg/Fe]. In the shortest timescale model, $\tau_\star = 0.5$ Gyr, [Mg/Fe] drops from $\sim$ 0.45 to 0.08 dex in 2 Gyr. In comparison, the longest timescale model, $\tau_\star = 5$ Gyr only drops to $\sim$ 0.2 dex in the same time.

The lower panel shows the negative of the time derivative of [Mg/Fe]. This panel shows the same behavior, with the slope of the $\tau_\star = 0.5\,\mathrm{Gyr}$ model peaking at $-0.5\,\mathrm{dex/Gyr}$ compared to the 5 Gyr model which peaks at $-0.25\,\mathrm{dex/Gyr}$. After 1 Gyr, the trend starts to reverse, with the longer SF timescale models declining more rapidly, though at a much reduced rate ($\sim -0.1\,\mathrm{dex/Gyr}$) than at the peak.

4. DISCUSSION

In Figure 1, we compared the abundance plane between the Milky Way and our SoI before and after the α-enhancement. It is visibly obvious that the TNG SoI is unimodal before the α-enhancement and bimodal afterwards (ignoring the minor mode at high-[Mg/Fe]). Here, we briefly discuss two main points: (1) assuming the α-enhancement is justified, what leads to the bimodality in the SoI?, and (2) what justifies the α-enhancement? We then briefly extend our comparison to the Milky Way data.

4.1. *Cause of Bimodality*

An extensive analysis of our SoI is beyond the scope of this project, but here we argue that the evidence is consistent with the scenario presented in Beane (2024). They presented an idealized simulation resembling the merger between the Milky Way and GSE. They varied the orbital parameters slightly in a grid of 27 simulations and found that simulations which had a brief quiescent period as a result of the merger led to a bimodal abundance distribution. They argued that AGN activity was responsible for this brief quenching.

Once the α-enhancement post-processing has been done, the SoI that we have studied in this work is consistent with this scenario. The vertical dashed line in Figures 2 and 3 denotes the transition between the high- and low-α sequences. We place it at an age of 10.75 Gyr or a formation time of $\sim 3\,\mathrm{Gyr}$. The upper right panel of Figure 2 shows 2D histograms of [Mg/Fe] vs star particle age in fixed bins of [Fe/H] (each color is a different [Fe/H] bin, and an offset is given to [Mg/Fe] to avoid overlap). Stars which formed before the dashed line had a steep decline of [Mg/Fe] with time, while the relation in star particles formed after the dashed line is much more flat. At the line, we see a gap in the $[\mathrm{Fe/H}] = -0.5$ and -0.25 bins.

The age gap in each [Fe/H] bin of Figure 2 is contemperaneous with a minimum in the global SFR. We can see in the upper panel of Figure 3 that this dashed line lies almost exactly at the point of a local minimum in the SFH. This minimum, which is $\sim 10\,M_\odot/\mathrm{yr}$, is 6–7× smaller than the maxima before and after it.[1]

During this period of suppressed SF, we argue that the relative lack of enrichment of Type II SNe which leads to a lower rate of Mg production. This leads to a rapid reduction in [Mg/Fe]. This, combined with a lack of SF in the first place, leads to a scarcity of star particles in the region intermediate between the high- and low-α sequences. A more in-depth explanation is given in Section 4.1 in Beane (2024).

In the fiducial TNG distribution shown in the upper middle panel of Figure 2, the same general behavior with respect to the dashed line is present. However, because the [Mg/Fe] decline before the dashed line is not as strong, star particles which formed before and after the dashed line overlap in the [Mg/Fe] distribution shown in Figure 1.

It is also worth noting that in both the fiducial and α-enhanced SoI, there is a sort of rebound effect in [Mg/Fe]. The star particles which form directly after the dashed line have a slightly lower [Mg/Fe] than stars which form after. This was seen in Figure 9 of Beane (2024). In that work, it was argued that this occurs because, during the period of suppressed SF, the $[\alpha/\mathrm{Fe}]$ of star forming gas plummets since there is no contribution from Type II SNe. Later, the $[\alpha/\mathrm{Fe}]$ of the gas will recover when the SFR also recovers, but there is a brief window when old, low-α stars can form.

4.2. *Steepening of α Decline*

As described in Section **??**, we applied a post-processing to the [Mg/Fe] of star particles in the TNG simulation. Specifically, for star particles formed before $z = 1.5$, we added to their [Mg/Fe] a value of $0.1 \times (t_{1.5} - t_{\mathrm{form}})$, where $t_{1.5}$ is the age of the universe at $z = 1.5$ ($\sim 4.3\,\mathrm{Gyr}$) and t_{form} is the formation time. This post-processed subhalo is presented alongside the fiducial subhalo in the right and middle columns, respectively, of Figures 1 and 2.

The [Mg/Fe] value of star forming gas is the result of a complicated mixture of many different aspects of the TNG model, to name a few: stellar and AGN feedback which alter gas inflows and outflows, secular, dynamical evolution, SF prescription, magnetic fields, (lack of) cosmic rays, diffusivity of hydrodynamics solver, and, of course, enrichment models. Isolating the cause of the "incorrect"[2] [Mg/Fe] vs time evolution at high-z is not straightforward nor, in our opinion, even possible. However, we do offer one reasonable explanation – the SFE at high densities, more present at high-z, is too low.

[1] A reasonable argument can be made that $10\,M_\odot/\mathrm{yr}$ is hardly quiescent. However, for our purposes, it only matters that the SFR at the minimum is small relative to the SFR close in time before and after.

[2] Our case study of a single galaxy, selected in a non-reproducible manner, is hardly cause to firmly assert that the fiducial evolution in TNG50 is incorrect.

We demonstrate the impact of the SFE on the [α/Fe] ratio using a simple one-zone chemical evolution model with the publicly available code `VICE`. The details of our setup is given in Section 2.3. We vary the SF timescale, $\tau_\star = M_{\rm gas}/{\rm SFR}$, and examine the impact on the [Mg/Fe] ratio as a function of time. We find that shorter SF timescales do lead to a more rapid reduction in [Mg/Fe]. The rate of decrease in [Mg/Fe], at its maximum, varies from ~ -0.25 dex/Gyr in the $\tau_\star = 5$ Gyr model to ~ -0.5 dex/Gyr in the $\tau_\star = 0.5$ Gyr model. For our post-processing, assumed an additional decrease rate of 0.1 dex/Gyr. Such a difference is well within the range of [Mg/Fe] decrease seen in our different $\tau_\star$ models.

S. Hassan et al. (in preparation) demonstrated that the pressure regulated feedback model of Ostriker & Kim (2022) predicts higher SFRs of patches of gaseous disks in TNG50 than the fiducial model by up to an order of magnitude. This is well within our needed factor of 2 in $\tau_\star$. Therefore, our argument that the [Mg/Fe] does not decline quickly enough at high-z is reasonably justified. An intuitive understanding of the impact the decline in [α/Fe] vs time has is that, when [α/Fe] declines rapidly, it is a better estimator of age. When it is a better estimator of age, events which are separated temporally become better separated in the abundance plane.

4.3. *Comparison to Observations*

The lower left panel of Figure 2 shows the [Mg/Fe] vs age of stars in bins of [Fe/H] which pass our solar neighborhood selection and are present in the APOKASC2 catalog. In the bins where the bimodality is strongest (blue and orange, [Fe/H] = -0.5 and -0.25, respectively), we see that there is a sort of two tiered distribution with significant overlap in age. In the SoI with age and abundance errors shown in the lower right panel, a very similar distribution can be seen in all [Fe/H] bins. An examination of the true distribution in the SoI (upper right panel), we see that the two distributions are in fact very cleanly separated in age. We do not know the true underlying distribution in the Milky Way, but these panels show that the general picture shown in our SoI is consistent with the Milky Way.

4.4. *Cause of Quiescence*

It is natural to question why the minimum in the SFR occurs. In Beane (2024), AGN activity from a merger was the suspected cause. Here, we can see that there is indeed a brief burst in AGN accretion at the time of the merger (middle panel of Figure 3). Establishing a causal relationship between the two is beyond the scope of the present work, though it is the same suspected cause as in Beane (2024).

5. CONCLUSIONS

In this work, we examined a specific subhalo in Illustris TNG50. This subhalo is at a Milky Way-progenitor mass at high-z ($z \sim 2$). After applying a post-processing step that increased the [Mg/Fe] of star particles formed before $z = 1.5$, this subhalo hosts a strong bimodality in the plane of [Mg/Fe] and [Fe/H], shown in Figure 1. This post-processing is justified by arguing that the SFE of dense gas is too low in TNG (Section 4.2).

This bimodality can be traced to an event that occurred at an age of 10.75 Gyr, or formation time of ~ 3 Gyr ($z \sim 2$). Shown as a vertical dashed line in Figure 2, star particles which form before this form at high-α while stars which form after form at lower α. At the dashed line, there is a gap. We argue that the presence of this gap is responsible for the valley in the bimodality (Figure 1). It is accompanied by a global reduction in the SFR by about a factor of 6 (upper panel of Figure 3).

The reduction in the SFR has two effects. First, a lower production of Mg is the natural result of a lack of Type II SNe. Second, the lack of SF means that stars at [Mg/Fe] intermediate between the high- and low-α sequences never form. This is the same argument that was first presented in Beane (2024). When observational errors are added to the subhalo's abundance vs age distribution, we show that it is broadly consistent with the Milky Way's abundance-age distribution (Section 4.3).

This work adds further support that the argument made in Beane (2024) is a plausible explanation for the Milky Way's abundance bimodality.

This work has made use of data from the European Space Agency (ESA) mission *Gaia* (https://www.cosmos.esa.int/gaia), processed by the *Gaia* Data Processing and Analysis Consortium (DPAC, https://www.cosmos.esa.int/web/gaia/dpac/consortium). Funding for the DPAC has been provided by national institutions, in particular the institutions participating in the *Gaia* Multilateral Agreement.

REFERENCES

Adibekyan, V. Z., Santos, N. C., Sousa, S. G., & Israelian, G. 2011, A&A, 535, L11, doi: 10.1051/0004-6361/201118240

Adibekyan, V. Z., Sousa, S. G., Santos, N. C., et al. 2012, A&A, 545, A32, doi: 10.1051/0004-6361/201219401

Beane, A. 2024, arXiv e-prints, arXiv:2407.07985, doi: 10.48550/arXiv.2407.07985

Belokurov, V., Erkal, D., Evans, N. W., Koposov, S. E., & Deason, A. J. 2018, MNRAS, 478, 611, doi: 10.1093/mnras/sty982

Bensby, T., Feltzing, S., & Oey, M. S. 2014, A&A, 562, A71, doi: 10.1051/0004-6361/201322631

Beraldo e Silva, L., Debattista, V. P., Khachaturyants, T., & Nidever, D. 2020, MNRAS, 492, 4716, doi: 10.1093/mnras/staa065

Beraldo e Silva, L., Debattista, V. P., Nidever, D., Amarante, J. A. S., & Garver, B. 2021, MNRAS, 502, 260, doi: 10.1093/mnras/staa3966

Bland-Hawthorn, J., & Gerhard, O. 2016, ARA&A, 54, 529, doi: 10.1146/annurev-astro-081915-023441

Brook, C., Richard, S., Kawata, D., Martel, H., & Gibson, B. K. 2007, ApJ, 658, 60, doi: 10.1086/511056

Brook, C. B., Gibson, B. K., Martel, H., & Kawata, D. 2005, ApJ, 630, 298, doi: 10.1086/431924

Brook, C. B., Kawata, D., Gibson, B. K., & Freeman, K. C. 2004, ApJ, 612, 894, doi: 10.1086/422709

Buck, T. 2020, MNRAS, 491, 5435, doi: 10.1093/mnras/stz3289

Chen, B., Hayden, M. R., Sharma, S., et al. 2023, MNRAS, 523, 3791, doi: 10.1093/mnras/stad1568

Chiappini, C. 2009, in The Galaxy Disk in Cosmological Context, ed. J. Andersen, Nordströara, B. m, & J. Bland-Hawthorn, Vol. 254, 191–196, doi: 10.1017/S1743921308027580

Chiappini, C., Matteucci, F., & Gratton, R. 1997, ApJ, 477, 765, doi: 10.1086/303726

Ciucă, I., Kawata, D., Ting, Y.-S., et al. 2024, MNRAS, 528, L122, doi: 10.1093/mnrasl/slad033

Clarke, A. J., Debattista, V. P., Nidever, D. L., et al. 2019, MNRAS, 484, 3476, doi: 10.1093/mnras/stz104

Fuhrmann, K. 1998, A&A, 338, 161

—. 2004, Astronomische Nachrichten, 325, 3, doi: 10.1002/asna.200310173

García Pérez, A. E., Allende Prieto, C., Holtzman, J. A., et al. 2016, AJ, 151, 144, doi: 10.3847/0004-6256/151/6/144

Garver, B. R., Nidever, D. L., Debattista, V. P., Beraldo e Silva, L., & Khachaturyants, T. 2023, ApJ, 953, 128, doi: 10.3847/1538-4357/acdfc6

Gratton, R., Carretta, E., Matteucci, F., & Sneden, C. 1996, in Astronomical Society of the Pacific Conference Series, Vol. 92, Formation of the Galactic Halo...Inside and Out, ed. H. L. Morrison & A. Sarajedini, 307

Grisoni, V., Spitoni, E., Matteucci, F., et al. 2017, MNRAS, 472, 3637, doi: 10.1093/mnras/stx2201

Hayden, M. R., Bland-Hawthorn, J., Sharma, S., et al. 2020, MNRAS, 493, 2952, doi: 10.1093/mnras/staa335

Helmi, A., Babusiaux, C., Koppelman, H. H., et al. 2018, Nature, 563, 85, doi: 10.1038/s41586-018-0625-x

Khoperskov, S., Haywood, M., Snaith, O., et al. 2021, MNRAS, 501, 5176, doi: 10.1093/mnras/staa3996

Naidu, R. P., Conroy, C., Bonaca, A., et al. 2020, ApJ, 901, 48, doi: 10.3847/1538-4357/abaef4

Nelson, D., Pillepich, A., Springel, V., et al. 2019, MNRAS, 490, 3234, doi: 10.1093/mnras/stz2306

Nidever, D. L., Bovy, J., Bird, J. C., et al. 2014, ApJ, 796, 38, doi: 10.1088/0004-637X/796/1/38

Ostriker, E. C., & Kim, C.-G. 2022, ApJ, 936, 137, doi: 10.3847/1538-4357/ac7de2

Pakmor, R., Springel, V., Bauer, A., et al. 2016, MNRAS, 455, 1134, doi: 10.1093/mnras/stv2380

Pillepich, A., Springel, V., Nelson, D., et al. 2018, MNRAS, 473, 4077, doi: 10.1093/mnras/stx2656

Pillepich, A., Nelson, D., Springel, V., et al. 2019, MNRAS, 490, 3196, doi: 10.1093/mnras/stz2338

Pinsonneault, M. H., Elsworth, Y. P., Tayar, J., et al. 2018, ApJS, 239, 32, doi: 10.3847/1538-4365/aaebfd

Reddy, B. E., Lambert, D. L., & Allende Prieto, C. 2006, MNRAS, 367, 1329, doi: 10.1111/j.1365-2966.2006.10148.x

Richard, S., Brook, C. B., Martel, H., et al. 2010, MNRAS, 402, 1489, doi: 10.1111/j.1365-2966.2009.16008.x

Schönrich, R., & Binney, J. 2009, MNRAS, 396, 203, doi: 10.1111/j.1365-2966.2009.14750.x

Sharma, S., Hayden, M. R., & Bland-Hawthorn, J. 2021, MNRAS, 507, 5882, doi: 10.1093/mnras/stab2015

Spitoni, E., Silva Aguirre, V., Matteucci, F., Calura, F., & Grisoni, V. 2019, A&A, 623, A60, doi: 10.1051/0004-6361/201834188

Springel, V. 2010, MNRAS, 401, 791, doi: 10.1111/j.1365-2966.2009.15715.x

van Dokkum, P. G., Leja, J., Nelson, E. J., et al. 2013, ApJL, 771, L35, doi: 10.1088/2041-8205/771/2/L35

Vogelsberger, M., Genel, S., Sijacki, D., et al. 2013, MNRAS, 436, 3031, doi: 10.1093/mnras/stt1789

Weinberger, R., Springel, V., Hernquist, L., et al. 2017, MNRAS, 465, 3291, doi: 10.1093/mnras/stw2944

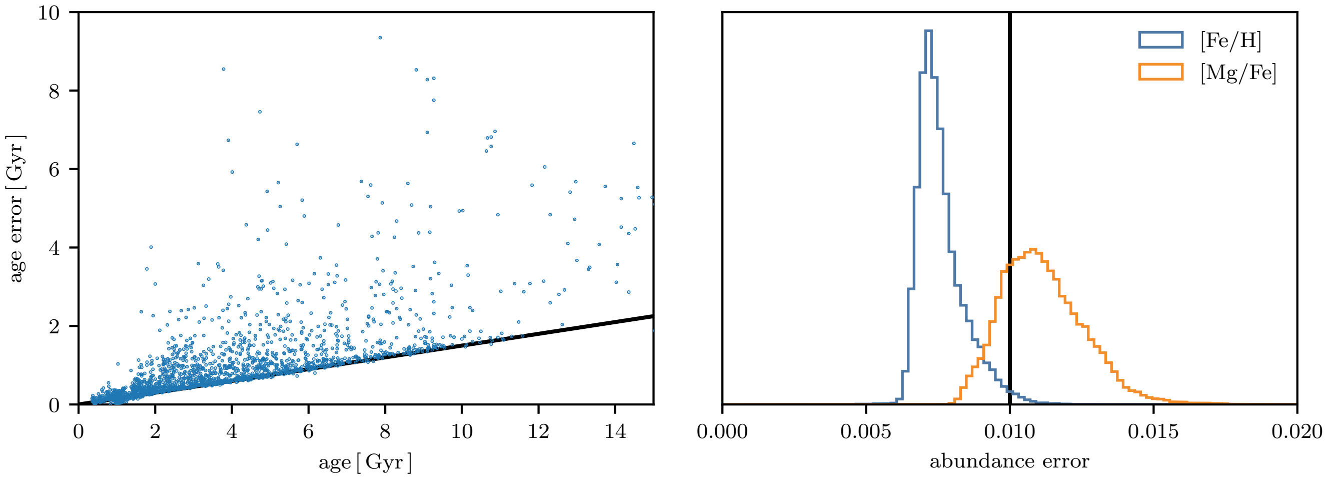

Figure 5. The observational errors of the APOKASC2 (left) and ASPCAP dataset (right). We show, on the left, a line indicating a 15% error in observed age and on the right a vertical line indicating a 0.01 dex error.

APPENDIX

A. OBSERVATIONAL ERRORS

In Figure 2, we assumed observational errors of 15% in age and 0.01 dex in [Mg/Fe]. In Figure 5, we plot the quoted observational errors of the APOKASC2 (left) and ASPCAP (right) datasets, showing both [Fe/H] and [Mg/Fe] (blue and orange, respectively). We show our 15% age error and 0.01 dex abundance error assumptions as black lines. For the age error, we used the maximum of the upper and lower estimates from Pinsonneault et al. (2018). Our assumed errors are generally consistent with the errors. Our error in [Mg/Fe] is a bit smaller than in ASPCAP, but the age estimates are by far the more constraining of the two.